ATLAS NOTE

ATLAS-CONF-2012-147

November 9, 2012

Search for New Phenomena in Monojet plus Missing Transverse Momentum Final States using 10 fb^{-1} of pp Collisions at $\sqrt{s} = 8$ TeV with the ATLAS detector at the LHC

ATLAS Collaboration

Abstract

We report preliminary results on a search for new phenomena in monojet plus large missing transverse momentum final states. The analysis uses 10.5 fb^{-1} of $\sqrt{s} = 8$ TeV data collected in 2012 with the ATLAS detector at the LHC. Good agreement is observed between the number of events in data and the Standard Model predictions. The results are translated into new limits on the production of light gravitinos in association with gluinos or scalar quarks in a gauge-mediated supersymmetric model, leading to the best lower bound to date on the gravitino mass. Exclusion limits on models with large extra spatial dimensions and on pair production of weakly interacting dark matter candidates are also presented.

ATLAS-CONF-2012-147
12 November 2012

1 Introduction

Events with an energetic jet of hadrons and large missing momentum in the final state constitute a clean and distinctive signature in searches for new physics at colliders. In particular, monojet (and monophoton) final states have been studied [1–14] in the context of searches for supersymmetry (gravitinos), large extra spatial dimensions (LED) aiming to provide a solution to the mass hierarchy problem, and the search for weakly interacting massive particles (WIMPs) as candidates for dark matter (DM).

The Arkani-Hamed, Dimopoulos, and Dvali (ADD) model for LED [15] explains the large difference between the electroweak unification scale $O(10^2)$ GeV and the Planck scale $M_{Pl} \sim O(10^{19})$ GeV by postulating the presence of n extra spatial dimensions of size R, and defining a fundamental Planck scale in $4 + n$ dimensions, M_D, given by ${M_{Pl}}^2 \sim {M_D}^{2+n} R^n$. An appropriate choice of R for a given n yields a value of M_D at the electroweak scale. The extra spatial dimensions are compactified, resulting in a Kaluza-Klein tower of massive graviton modes. At hadron colliders, these graviton modes may escape detection and can be produced in association with an energetic jet, leading to a monojet signature in the final state.

The presence of a non-baryonic DM component in the universe is inferred from the observation of its gravitational interactions (see ref. [16] for a review), although its nature is otherwise unknown. A WIMP χ with mass m_χ in the range between 1 GeV and a few TeV is a plausible candidate for DM. It could be detected via its scattering with heavy nuclei [17–21], the detection of cosmic rays (energetic photons, electrons, positrons, protons, antiprotons, or neutrinos) from $\chi\bar{\chi}$ annihilation in astrophysical sources [16], or via $\chi\bar{\chi}$ pair-production at colliders where the WIMPs do not interact with the detector and the event is identified by the presence of an energetic jet from initial-state radiation. Here, the interaction of WIMPs with Standard Model (SM) particles will be assumed to be driven by a mediator with mass at the TeV scale and described using a non-renormalizable effective theory [22] with several operators. The vertex coupling is suppressed by an effective cut-off mass scale M_*.

In gauge-mediated SUSY breaking (GMSB) scenarios [23–25], the gravitino $\tilde{G}$ (spin-$\frac{3}{2}$ superpartner of the graviton) is often considered the lightest supersymmetric particle (LSP) and a potential candidate for DM, where its mass is related to the SUSY breaking scale F and M_{Pl} via $m_{\tilde{G}} \propto F/M_{Pl}$ [23]. At hadron colliders, in low-scale SUSY breaking scenarios with very light gravitinos, the cross section for associate production of gravitino-squark ($pp \to \tilde{G}\tilde{q} + X$) and gravitino-gluino ($pp \to \tilde{G}\tilde{g} + X$) processes become relevant [26]. The cross section depends on $m_{\tilde{G}}$ as $\sigma \sim 1/m^2_{\tilde{G}}$ and therefore provides the means to determine a lower bound on $m_{\tilde{G}}$. The decay of the gluino or squark into a gravitino and a gluon ($\tilde{g} \to \tilde{G}g$) or a gravitino and a quark ($\tilde{q} \to \tilde{G}q$), respectively, dominates [26], and the final state is characterized by the presence of a pair of gravitinos that escape detection and an energetic jet, leading to a monojet topology. Previous studies at colliders [14, 27], using monophoton and monojet final states, considered the production of gravitinos in association with a photon or a jet in the final state, respectively, and assumed extremely heavy squarks and gluinos. Within this approximation, they established a lower limit for the gravitino mass of $m_{\tilde{G}} > 1.37 \cdot 10^{-5}$ eV.

This note reports results of the search for new phenomena in monojet final states, based on $\sqrt{s} =$ 8 TeV proton-proton collision data corresponding to an integrated luminosity of 10.5 fb^{-1} collected with the ATLAS detector [28, 29] at the LHC during 2012. The note is organized as follows. Section 2 provides details on the identification of leptons and jets of hadrons in the final state. The event selection is presented in Section 3. Section 4 describes the Monte Carlo (MC) simulations used in the analysis, while Section 5 discusses the estimation of the SM background predictions. Section 6 presents the final results and their interpretation in terms of the ADD LED model, the pair production of WIMPs, and the production of light gravitinos. Finally, Section 7 is devoted to summary and conclusions.

2 Reconstruction of physics objects

In this analysis, jets are reconstructed from energy deposits in calorimeters using the anti-k_t jet algorithm [30] with the distance parameter set to $R = 0.4$. The measured jet transverse momentum p_{T}[1] is corrected for detector effects, including non-compensation of hadronic showers, and for contributions from multiple proton-proton interactions per beam bunch crossing (pileup), as described in ref. [31]. The magnitude of the missing transverse momentum, $E_{\mathrm{T}}^{\mathrm{miss}}$, is reconstructed using all locally-calibrated energy deposits in the calorimeter up to pseudorapidity $|\eta|$ of 4.9. These clusters are calibrated taking into account the difference in response of hadrons compared to electrons or photons, as well as dead material and out-of-cluster energy losses [32].

Events with identified leptons (electrons and muons) in the final state are vetoed in the nominal selection criteria (see next section) to suppress top and electroweak background processes. In addition, the presence of leptons in the final state is used to define data control samples and validate the MC predictions for the remaining background contributions. Electron candidates are required to have $p_{\mathrm{T}} > 20$ GeV and $|\eta| < 2.47$, and to pass the *medium* electron shower shape and track selection criteria described in ref. [33]. Muon candidates are required to have $p_{\mathrm{T}} > 7$ GeV and $|\eta| < 2.5$ and to pass the *combined* reconstruction criteria described in [33], which include the association of a stand-alone muon spectrometer track to an inner detector track.

Possible overlaps between identified leptons and jets in the final state are resolved. Jets are discarded if their distance ΔR ($\eta - \phi$ space) to an identified electron is less than 0.2. For the remaining jets in the events the electrons between 0.2 and 0.4 from a jet are removed. Muons are required to be isolated: the sum of the transverse momenta of the tracks not associated with the muon in a cone of radius 0.2 around the muon direction is required to be less than 1.8 GeV.

3 Event selection

The data sample considered in this note was collected with operational ATLAS tracking, calorimeters, muon chambers, and magnets, and corresponds to a total integrated luminosity of 10.5 fb^{-1}. The data were selected online using a trigger logic that selects events with missing transverse momentum $E_{\mathrm{T}}^{\mathrm{miss}}$ above 80 GeV, as computed at the final stage of the three-level trigger system of ATLAS [34]. The trigger selection is more than 95% efficient for offline reconstructed $E_{\mathrm{T}}^{\mathrm{miss}} > 120$ GeV, as determined using an unbiased data sample with muons in the final state. The offline event selection criteria applied follow closely those in ref. [12]:

- Events are required to have a reconstructed primary vertex. This rejects beam-related backgrounds and cosmic rays.
- Events are required to have $E_{\mathrm{T}}^{\mathrm{miss}} > 120$ GeV and at least one jet with $p_{\mathrm{T}} > 120$ GeV and $|\eta^{\mathrm{jet}}| < 2$ in the final state. Events with more than two jets with p_{T} above 30 GeV in the region $|\eta| < 4.5$ are rejected. An additional requirement on the azimuthal separation $\Delta\phi(\mathrm{jet}, E_{\mathrm{T}}^{\mathrm{miss}}) > 0.5$ between the $E_{\mathrm{T}}^{\mathrm{miss}}$ and the direction of the second leading jet (if found) is required, that reduces the QCD background contribution where the large $E_{\mathrm{T}}^{\mathrm{miss}}$ originates from the mis-measurement of the second-leading jet p_{T}.

[1] ATLAS uses a right-handed coordinate system with its origin at the nominal interaction point (IP) in the centre of the detector and the z-axis along the beam pipe. The x-axis points from the IP to the centre of the LHC ring, and the y-axis points upward. Polar coordinates (r, ϕ) are used in the transverse (x,y)-plane, ϕ being the azimuthal angle around the beam pipe. The pseudorapidity is defined in terms of the polar angle θ as $\eta = -\ln\tan(\theta/2)$.

- Events are rejected if they contain any jet with $p_{\mathrm{T}} > 20$ GeV and $|\eta| < 4.5$ that present anomalous charged fraction f_{ch} [2], electromagnetic fraction f_{em} in the calorimeter, or timing (as determined from the energy deposits of the jet constituents) inconsistent with the requirement that they originate from a proton-proton collision, and most likely produced by beam-related backgrounds and cosmic rays. In addition, the highest p_{T} jet selected (see above) is required to have $f_{\mathrm{ch}} > 0.2$, $f_{\mathrm{em}} > 0.1$, and $f_{\mathrm{max}} < 0.8$[3]. Additional requirements are applied to suppress coherent noise and electronic noise bursts in the calorimeter producing anomalous energy deposits [35].

- Events are required to have no identified electrons or muons according to the selection criteria stated in the previous section.

Four different signal regions (here denoted as SR1 to SR4) are defined with increasing lower thresholds on the leading jet p_{T} and $E_{\mathrm{T}}^{\mathrm{miss}}$ which vary from 120 GeV to 500 GeV (see Table 1).

Selection criteria				
Primary vertex				
$E_{\mathrm{T}}^{\mathrm{miss}} > 120$ GeV				
Jet cleanup requirements				
Leading jet with $p_{\mathrm{T}} > 120$ GeV and $\|\eta\| < 2.0$				
At most two jets with $p_{\mathrm{T}} > 30$ GeV and $\|\eta\| < 4.5$				
$\Delta\phi(\mathrm{jet}, E_{\mathrm{T}}^{\mathrm{miss}}) > 0.5$ (second-leading jet)				
Lepton vetoes				
signal region	SR1	SR2	SR3	SR4
minimum leading jet p_{T} (GeV)	120	220	350	500
minimum $E_{\mathrm{T}}^{\mathrm{miss}}$ (GeV)	120	220	350	500
Events in data (10.5 fb^{-1})	350932	25515	2353	268

Table 1: Event selection criteria applied and the total number of events in data observed in each signal region.

4 Monte Carlo simulation

MC event samples are used to compute detector acceptance and reconstruction efficiencies for the signal and some of the background processes, and to estimate systematic uncertainties on the final results.

Samples of simulated Z ($\rightarrow \nu\bar{\nu}$)+jets, Z/γ^*($\rightarrow \ell^+\ell^-$)+jets, and W($\rightarrow \ell\nu$)+jets events are generated using [36], interfaced to [37] with [38], using CTEQ6L1 [39] parton distribution functions (PDFs). The samples are initially normalized to predictions for inclusive Drell-Yan and W production calculated to next-to-next-to-leading order (NNLO) in perturbative QCD as determined by the FEWZ [40, 41] program using MSTW2008 PDFs. These MC predictions are subsequently normalized using control samples in data as detailed below. Top-quark production samples are generated using @ [42] and CT10 [43] PDFs, while diboson processes are generated using S [44] and / normalized to next-to-leading-order (NLO) predictions with MRST2007 [45, 46] PDFs. Samples of multi-jets background contributions are simulated using LO perturbative QCD matrix elements for $2 \rightarrow 2$ processes plus parton shower in the leading logarithmic approximation, as implemented in [47] with MRST2007 PDFs.

[2] The charge fraction is defined as $f_{\mathrm{ch}} = \sum p_T^{\mathrm{track,jet}} / p_T^{\mathrm{jet}}$, where $\sum p_T^{\mathrm{track,jet}}$ is the scalar sum of the transverse momenta of tracks associated with the primary vertex within a cone of radius $R = 0.4$ around the jet axis, and p_T^{jet} is the transverse momentum as determined from calorimetric measurements.

[3] f_{max} denotes the maximum fraction of the jet energy collected by a single calorimeter layer.

MC simulated samples for the ADD LED model with different number of extra dimensions varying from 2 to 6 and M_D in the range 2 – 5 TeV are generated using the 8 program with CTEQ6.6 [48] PDFs, and renormalization and factorization scales set to $\sqrt{\frac{1}{2}m_G^2 + p_T^2}$, where m_G is the graviton mass and p_T denotes the transverse momentum of the recoiling parton.

Simulated events corresponding to the $p\bar{p} \to \chi\bar{\chi}q + X$ and $p\bar{p} \to \chi\bar{\chi}g + X$ processes with a minimum parton p_{T} of 80 GeV are generated using LO matrix elements from [49] interfaced to using CTEQ6L1 PDFs. The renormalization and factorization scales are set to the sum of $\sqrt{m^2 + p_T^2}$ for all the particles in the final state. In this analysis, WIMPs are assumed to be Dirac fermions and different vertex operators are considered, corresponding to the $qq \to \chi\chi$ operator D5 (vector) and the $gg \to \chi\chi$ operator D11 (scalar) in ref. [22].

Finally, MC simulated samples for gravitino production in association witn a gluino or a squark in the final state, $p\bar{p} \to \tilde{G}\tilde{g} + X$ and $p\bar{p} \to \tilde{G}\tilde{q} + X$, are generated using LO matrix elements in [50] interfaced with and using CTEQ6L1 PDFs. The narrow width approximation (NWA) for the gluino and squark decays $\tilde{g} \to g\tilde{G}$ and $\tilde{q} \to q\tilde{G}$ is assumed. The renormalization and factorization scales are set to the average of the mass of the final state particles involved in the hard interaction $(m_{\tilde{G}} + m_{\tilde{q},\tilde{g}})/2 \simeq m_{\tilde{q},\tilde{g}}/2$. Values for $m_{\tilde{G}}$ in the range between 10^{-3} eV and 10^{-5} eV are considered for squark and gluino masses in the range 50 GeV – 2.6 TeV.

The MC samples are generated with minimum bias interactions overlaid on top of the hard-scattering event in order to account for the multiple proton-proton interactions in the same beam crossing (pile-up) experienced in the data. The MC also accounts for the effects of proton-proton interactions in the previous/following beam crossings (out of time pileup). The MC generated samples are then passed through a simulation [51] of the ATLAS detector and trigger, based on GEANT4 [52]. The simulated events are reconstructed and analyzed with the same analysis chain as for the data, the same trigger and event selection criteria, and re-weighted such that the distribution of the number of proton-proton interactions matches that of the data.

5 Background estimation

The expected background to the monojet signature is dominated by $Z(\to \nu\bar{\nu})$+jets and W+jets production, and includes contributions from $Z/\gamma^*(\to \ell^+\ell^-)$+jets ($\ell = e, \mu, \tau$), multijet, $t\bar{t}$, and diboson (WW, WZ, ZZ) processes. The W/Z plus jets backgrounds are estimated using MC event samples normalized using data in control regions. The remaining SM backgrounds from $t\bar{t}$ and dibosons are determined using Monte Carlo simulated samples, while the multijet background contribution is extracted from data. Finally, the potential contributions from beam-related background and cosmic rays are estimated using data.

5.1 Electroweak background

Following one of the data-driven methods employed in [12], control samples in data, orthogonal to the signal regions, with identified electrons or muons in the final state and with the same requirements on the jet p_{T}, subleading jet vetoes, and $E_{\mathrm{T}}^{\mathrm{miss}}$, are used to determine the W/Z+jets electroweak backgrounds from data. This reduces significantly the relatively large theoretical and experimental systematic uncertainties associated to purely MC-based predictions. A $W(\to \mu\nu)$+jets dominated control sample is defined using events with a muon with $p_{\mathrm{T}} > 7$ GeV and transverse mass [4] in the region 40 GeV $< m_{\mathrm{T}} <$ 100 GeV. Similarly, a $Z/\gamma^*(\to \mu^+\mu^-)$+jets control sample is selected requiring the presence of

[4] The transverse mass m_{T} is defined by the lepton and neutrino p_{T} and direction as $m_T = \sqrt{2p_{\mathrm{T}}^{\ell}p_{\mathrm{T}}^{\nu}(1 - \cos(\phi^{\ell} - \phi^{\nu}))}$, where the (x, y) components of the neutrino momentum are taken to be the same as the corresponding $E_{\mathrm{T}}^{\mathrm{miss}}$ components.

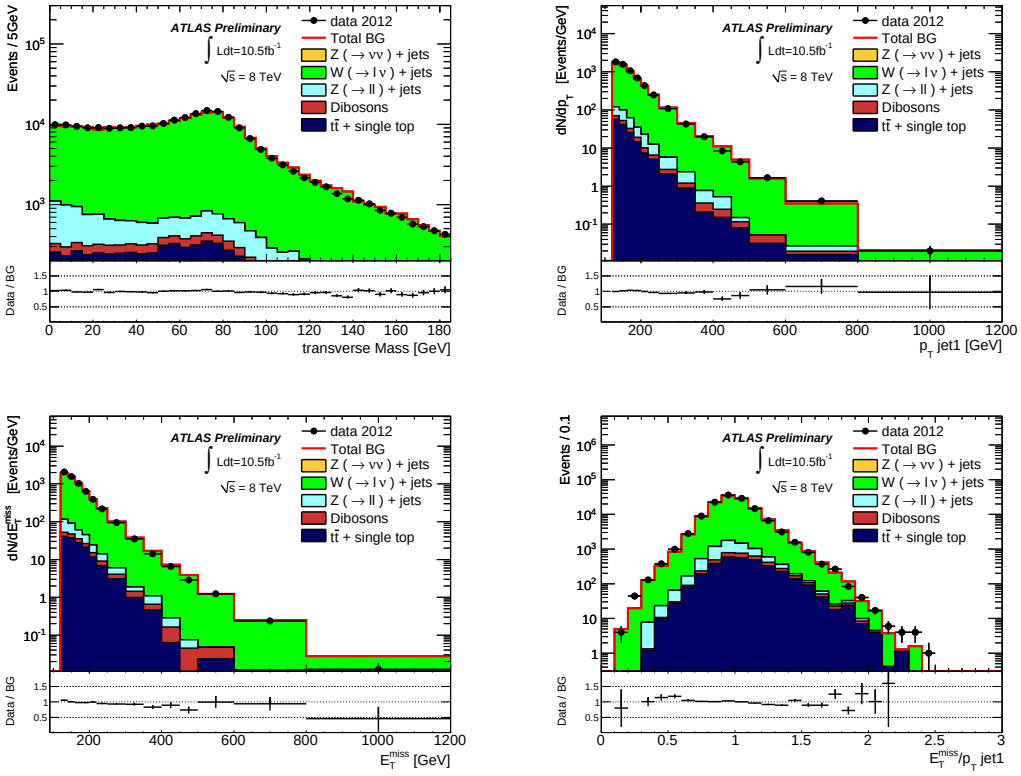

Figure 1: The measured transverse mass, leading jet p_{T}, $E_{\mathrm{T}}^{\mathrm{miss}}$, and $E_{\mathrm{T}}^{\mathrm{miss}}$ over leading jet p_{T} distributions in the $W(\rightarrow \mu\nu)$+jet control region, for the SR1 selection, compared to the background predictions. For illustration purposes, the W/Z+jet MC predictions are multiplied by a global scale factor 1.01 that brings the MC predictions close to the data in the control region, thus allowing a direct comparison of the shape of the measured and the simulated distributions.

two muons with invariant mass in the range 76 GeV $< m_{\mu\mu} <$ 116 GeV. Finally, a $W(\rightarrow e\nu)$+jets dominated control sample is defined using events with an electron candidate with $p_{\mathrm{T}} > 20$ GeV. Figures 1 to 3 show the measured distributions for the transverse mass or dilepton mass, leading jet p_{T}, $E_{\mathrm{T}}^{\mathrm{miss}}$, and $E_{\mathrm{T}}^{\mathrm{miss}}$ over leading jet p_{T} ratio in data and MC simulations in the different control samples for SR1 kinematics, where the W/Z+jets predictions are obtained using .

For each observable, bin-by-bin transfer factors, computed separately for the different electroweak background contributions, are defined for each of the signal regions. These transfer factors are then used to normalize the different electroweak background contributions, as determined by the simulation, in each of the signal regions. As an example, in the case of the dominant Z($\rightarrow \nu\bar{\nu}$)+jets background process, its contribution to a signal region in a given bin of a given distribution $N(\mathrm{Z}(\rightarrow \nu\bar{\nu}) + jets)_{signal}$ would be determined using the $W(\rightarrow \mu\nu)$+jets control sample in data according to

$$N(\mathrm{Z}(\rightarrow \nu\bar{\nu}) + jets)_{signal} = (N^{data}_{W\rightarrow\mu\nu,control} - N^{background}_{W,control}) \times \frac{N^{MC}(\mathrm{Z}(\rightarrow \nu\bar{\nu}) + jets)_{signal}}{N^{MC}_{W\rightarrow\mu\nu,control}}, \qquad (1)$$

where $N^{MC}(\mathrm{Z}(\rightarrow \nu\bar{\nu}) + jets)_{signal}$ denotes the background predicted by the MC simulation in the signal region, and $N^{data}_{W\rightarrow\mu\nu,control}$, $N^{MC}_{W\rightarrow\mu\nu,control}$, and $N^{background}_{W,control}$ denote, in the control region, the number of $W(\rightarrow \mu\nu)$+jets candidates in data and MC simulation, and the non-electroweak background contribution,

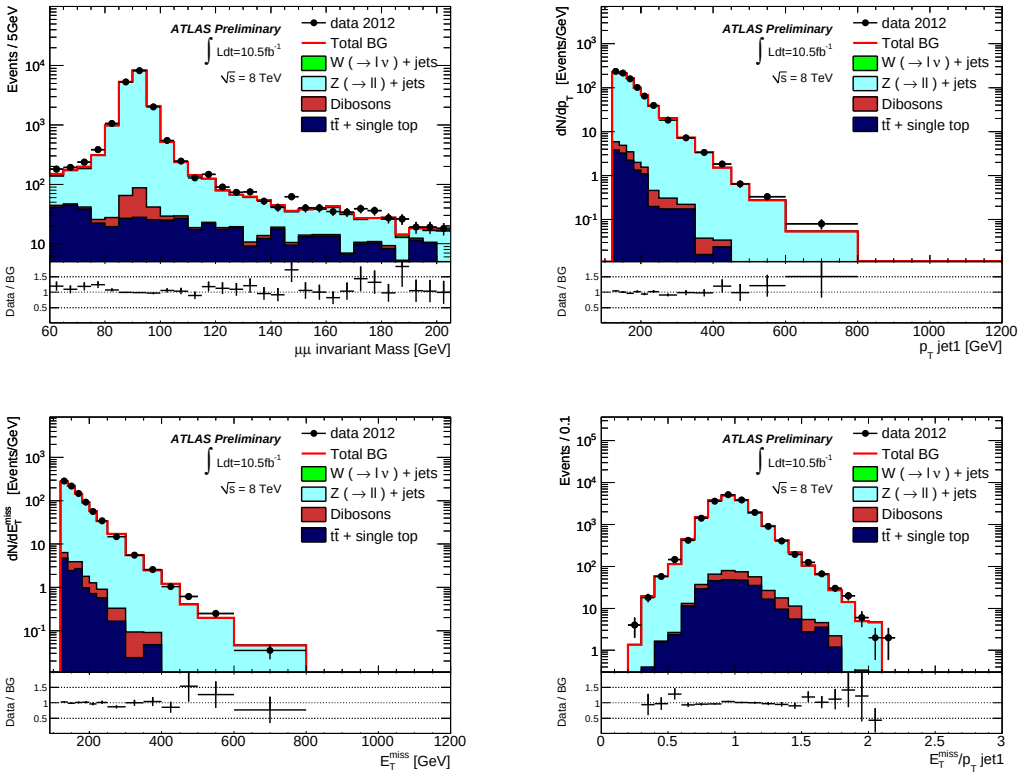

Figure 2: The measured dilepton invariant mass, leading jet p_{T}, $E_{\mathrm{T}}^{\mathrm{miss}}$, and $E_{\mathrm{T}}^{\mathrm{miss}}$ over leading jet p_{T} distributions in the Z/γ^{*} ($\rightarrow \mu^{+}\mu^{-}$)+jet control region, for the SR1 selection, compared to the background predictions. For illustration purposes, the W/Z+jet MC predictions are multiplied by a global scale factor 0.97 that brings the MC predictions close to the data in the control region, thus allowing a direct comparison of the shape of the measured and the simulated distributions.

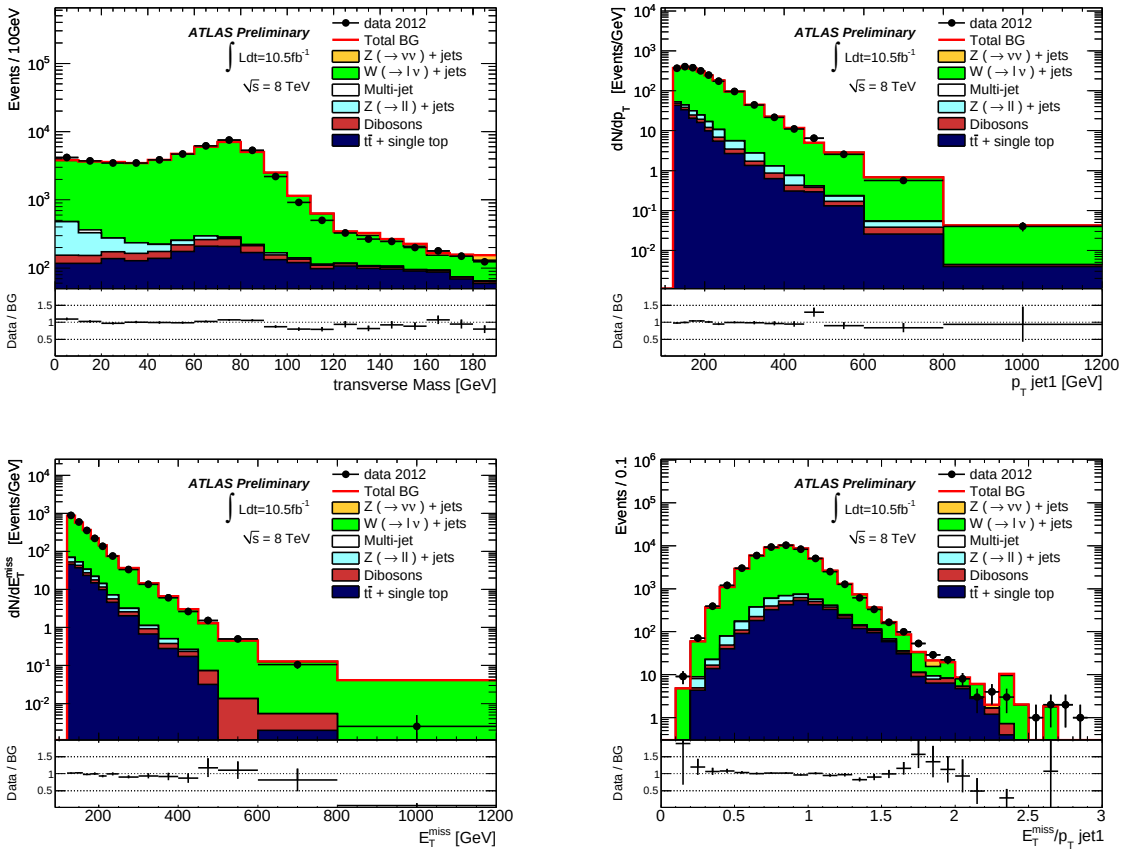

Figure 3: The measured transverse mass, leading jet p_{T}, $E_{\mathrm{T}}^{\mathrm{miss}}$, and $E_{\mathrm{T}}^{\mathrm{miss}}$ over leading jet p_{T} distributions in the $W(\rightarrow e\nu)$+jet control region, for the SR1 selection, compared to the background predictions. For illustration purposes, the W/Z+jet MC predictions are multiplied by a global scale factor 0.93 that brings the MC predictions close to the data in the control region, thus allowing a direct comparison of the shape of the measured and the simulated distributions.

respectively. The latter refer to top-quark and diboson processes and is computed using MC simulations. Therefore, the transfer factors for each process are defined as the ratio of simulated events for the process in the signal region over the total number of simulated events in the control region. As already mentioned, the same procedure is carried out to determine the rest of the electroweak background contributions in the different signal regions.

In this analysis, the $W(\rightarrow \mu\nu)$+jets control sample is employed to define transfer factors for all the electroweak processes, with the exception of $W(\rightarrow e\nu)$+jets, $Z/\gamma^*(\rightarrow \tau^+\tau^-)$+jets, and Z/γ^* $(\rightarrow e^+ e^-)$+jets contributions for which the $W(\rightarrow e\nu)$+jets control sample is used. If the Z/γ^* $(\rightarrow \mu^+ \mu^-)$+jets control sample is used instead of the $W(\rightarrow \mu\nu)$+jets control sample, consistent results are obtained. Similarly, consistent results are found for the $W(\rightarrow \tau\nu)$+jets background contribution when the $W(\rightarrow e\nu)$+jets control sample is used instead of the $W(\rightarrow \mu\nu)$+jets control sample.

Different sources of systematic uncertainty are considered in the determination of the electroweak background contributions. Uncertainties in the absolute jet and $E_{\mathrm{T}}^{\mathrm{miss}}$ energy scale and resolution [31] translate into an uncertainty on the transfer factors that varies between 2% and 4% as the leading-jet p_{T} and $E_{\mathrm{T}}^{\mathrm{miss}}$ increase. Uncertainties in the simulated lepton identification efficiencies translate into a 1% to 3% uncertainty in the transfer factors with increasing leading jet p_{T} and $E_{\mathrm{T}}^{\mathrm{miss}}$ requirements. A conservative 20% uncertainty on the non-electroweak processes translates into a less than 1% uncertainty on the electroweak background in the signal regions. Uncertainties related to the modeling of the parton shower and hadronization in the MC samples for the W/Z+jets processes were studied in detail in the previous analysis at $\sqrt{s} = 7$ TeV [12] and resulted into a 3% uncertainty on the electroweak background contributions in the signal regions. This uncertainty is expected to be similar at 8 TeV and much smaller that the current uncertainties from the MC statistics in regions SR3 and SR4 which are used to set limits. Other sources of uncertainty related to the trigger efficiency and the total luminosity determination cancel out in the data-driven method.

As already mentioned, top-quark and diboson production background contributions are determined from MC simulations with an uncertainty of about 20%. This includes uncertainties due to jet and $E_{\mathrm{T}}^{\mathrm{miss}}$ absolute energy scale and resolution, a 3.6% uncertaintly on the quoted luminosity and an assigned 10% uncertainty in the predicted top-quark and diboson production cross sections. These processes contribute less than 1% to the total background in the different signal regions.

5.2 Multijet background

In this analysis, the multijet background with large $E_{\mathrm{T}}^{\mathrm{miss}}$ originates mainly from the misreconstruction of the energy of a jet in the calorimeters. In such events, the $E_{\mathrm{T}}^{\mathrm{miss}}$ direction will generally be aligned with the undetected jet in the event. To estimate this background, jets-enriched data control samples are defined using the nominal selections without the veto on the third-leading jet and requiring $\Delta\phi(jet - E_{\mathrm{T}}^{\mathrm{miss}}) < 0.5$ for the second-leading (third-leading) jet in events with two (three) jets. Events with more than three jets with p_{T} above 30 GeV are excluded. Small contributions from the rest of the SM processes are subtracted according to the MC predictions. In the case of W/Z plus jets processes, the predictions are corrected with the normalization factors derived above for the relevant kinematic selections. As an example, Figure 4 shows, for the SR1 selection and before the $\Delta\phi(jet - E_{\mathrm{T}}^{\mathrm{miss}})$ requirement is applied, the $\Delta\phi(jet - E_{\mathrm{T}}^{\mathrm{miss}})$ distribution compared to the SM predictions for two- and three-jets final states. The region $\Delta\phi(jet - E_{\mathrm{T}}^{\mathrm{miss}}) < 0.5$ is dominated by the QCD muti-jets background. As expected, the QCD multijet MC simulation only provides a qualitative description of the data in this region and it is affected by limited MC statistics. The agreement observed between data and MC predictions for $\Delta\phi(jet - E_{\mathrm{T}}^{\mathrm{miss}}) > 0.5$, where the W/Z plus jets contributions dominate, constitutes a further validation of the normalization factors extracted from the data in the previous section.

The measured p_{T} distribution of the less energetic jet in the multijet enriched control samples ($\Delta\phi(jet - E_{\mathrm{T}}^{\mathrm{miss}}) < 0.5$) are used to estimate the multijet background in the analyses. In each case, the number of

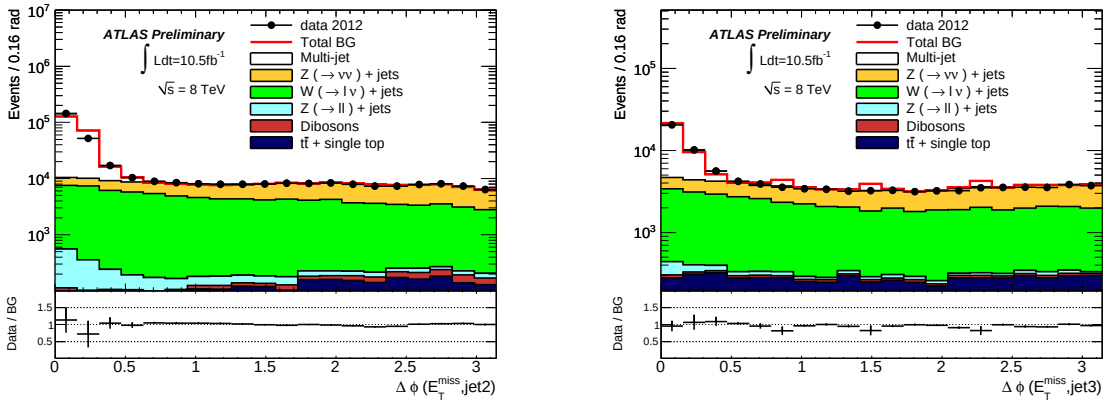

Figure 4: The measured $\Delta\phi(jet - E_{\mathrm{T}}^{\mathrm{miss}})$ distributions for the second leading jet (left) and third leading jet (right) in the SR1 region for events with two and three jets in the final state, respectively, before the jet vetoes are applied. The data are compared to the SM predictions, as determined by the MC simulation. The QCD jets predictions are determined from and include normalization factors 0.76 and 0.78 for the two and three jet case, respectively, that bring the predictions close to the data in the region $\Delta\phi(jet - E_{\mathrm{T}}^{\mathrm{miss}}) < 0.5$. The W/Z plus jets MC predictions contain the normalization factors extracted from the control data samples, as explained in the body of the text.

multijet background events is obtained from an extrapolation below the threshold of $p_{\mathrm{T}} = 30$ GeV. The multijet background estimation is performed separately for events with two and three jets in final state and added to obtain the final result. Several functional forms are considered to fit the data, and the difference is included in the systematic uncertainties, together with the uncertainties related to the subtraction of the rest of SM contributions. In the SR1 and SR2 analyses, a total of $6400 \pm 90(\mathrm{stat.}) \pm 5500(\mathrm{syst.})$ and $200 \pm 20(\mathrm{stat.}) \pm 200(\mathrm{syst.})$ multijet background events are expected, respectively, which constitute less than 1% of the total background. For the SR3 and SR4 analyses the multijet background is negligible.

5.3 Non-collision background

The jet cleanup cuts applied to the data sample in Section 3 are expected to maintain the non-collision background contribution below the percent level. An upper limit on the remaining non-collision background events in the signal region is obtained from data using the measured timing distribution of the leading jet and the events with a leading jet in the region -10 ns $< t < -5$ ns. The shape of the timing distribution for non-collision background events is reconstructed from a control data sample with relaxed jet cleanup cuts. The number of non-collision background events in the signal region $N_{\mathrm{NCB}}^{\mathrm{SR}}$ is computed as

$$N_{\mathrm{NCB}}^{\mathrm{SR}} = N_{-10<t<-5}^{\mathrm{SR}} \times \frac{N^{\mathrm{NCB}}}{N_{-10<t<-5}^{\mathrm{NCB}}}, \tag{2}$$

where $N_{-10<t<-5}^{\mathrm{SR}}$ and $N_{-10<t<-5}^{\mathrm{NCB}}$ denote the number of events in the signal region and non-collision background sample, respectively, with a leading jet in the range -10 ns $< t < -5$ ns, and N^{NCB} is the total number of events in the non-collision background sample. This results into $640 \pm 40(\mathrm{stat.}) \pm 60(\mathrm{syst.})$ and $22 \pm 7(\mathrm{stat.}) \pm 2(\mathrm{syst.})$ non-collision background events in the signal regions SR1 and SR2, respectively, while the non-collision background for SR3 and SR4 selections is negligible.

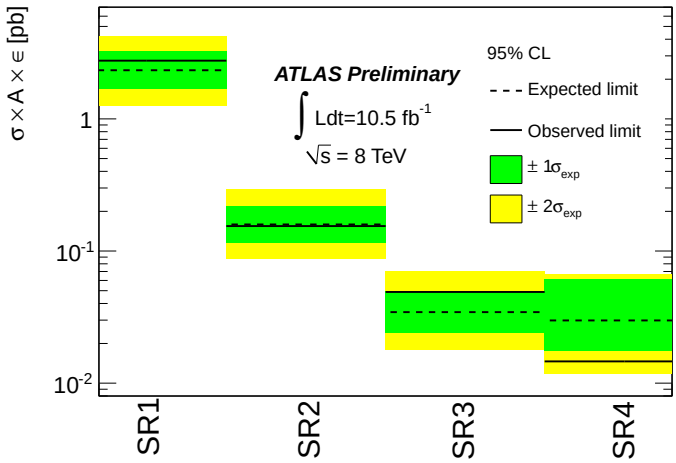

Figure 5: The model-independent observed (solid lines) and expected (dashed lines) 95% CL limits on $\sigma \times A \times \epsilon$ for the different signal regions. The shaded areas around the expected limit indicate the expected $\pm 1\sigma$ and $\pm 2\sigma$ ranges of limits in the absence of a signal.

6 Results

The expected background predictions are summarized in Table 2 for the SR1 to SR4 selections. Good agreement is observed between the data and the SM predictions. In the SR3 and SR4 regions the data is compatible with SM background predictions which suffer from sizeable statistical uncertainties. Based on the best expected limit, the region SR3 is used to compute limits on different models for physics beyond the SM in the following sections. Figures 6 and 7 show the measured leading jet p_{T} and $E_{\mathrm{T}}^{\mathrm{miss}}$ distributions for the different selections compared to the background predictions. For illustration purposes, the impact of different ADD, WIMP, and GMSB scenarios are included.

The agreement between the data and the SM predictions for the total number of events in the different analyses is translated into model-independent 95% confidence level (CL) upper limits on the visible cross section, defined as the production cross section times acceptance times efficiency ($\sigma \times A \times \epsilon$), using the CL_s modified frequentist approach [53] and considering the systematic uncertainties on the SM backgrounds (see Table 2) and a 3.6% uncertainty on the quoted integrated luminosity. The results are presented in Figure 5. Values of $\sigma \times A \times \epsilon$ above 2.8 pb, 0.16 pb, 0.05 pb, and 0.02 pb are excluded at 95% CL for SR1, SR2, SR3, and SR4 selections, respectively.

6.1 ADD large extra spatial dimensions

The results are translated into limits on the parameters of the ADD model. The typical $A \times \epsilon$ of the selection criteria vary, as n increases, between 21% and 24% for SR1 and between 1% to 2% for SR4, and are approximately independent of M_D.

Different sources of systematic uncertainty on the predicted ADD signals are considered. Experimental uncertainties related to the jet and $E_{\mathrm{T}}^{\mathrm{miss}}$ scales and resolutions introduce uncertainties in the signal yields that vary between 6% and 5% for SR1 and between 14% and 8% for SR4, with increasing n. In addition, a 1% uncertainty on the simulated trigger efficiency and a 3.6% uncertainty on the integrated luminosity are included. Uncertainties related to the modeling of the initial- and final-state gluon radiation (ISR and FSR) are determined using simulated samples with modified parton shower parameters. They translate into uncertainties on the ADD signal yields that vary between 5% and 8% in

Background Predictions ± (stat.data)± (stat.MC) ± (syst.)				
	SR1	SR2	SR3	SR4
$Z(\to \nu\bar{\nu})$+jets	173600 ± 500 ± 1300 ± 5500	15600 ± 200 ± 300 ± 500	1520 ± 50 ± 90 ± 60	270 ± 30 ± 40 ± 20
$W \to \tau\nu$+jets	87400 ± 300 ± 800 ± 3700	5580 ± 60 ± 190 ± 300	370 ± 10 ± 40 ± 30	39 ± 4 ± 11 ± 2
$W \to e\nu$+jets	36700 ± 200 ± 500 ± 1500	1880 ± 30 ± 100 ± 100	112 ± 5 ± 18 ± 9	16 ± 2 ± 6 ± 2
$W \to \mu\nu$+jets	34200 ± 100 ± 400 ± 1600	2050 ± 20 ± 100 ± 130	158 ± 5 ± 21 ± 14	42 ± 4 ± 13 ± 8
$Z \to \tau\tau$+jets	1263 ± 7 ± 44 ± 92	54 ± 1 ± 9 ± 5	1.3 ± 0.1 ± 1.3 ± 0.2	1.4 ± 0.2 ± 1.5 ± 0.2
$Z/\gamma^*(\to \mu^+\mu^-)$+jets	783 ± 2 ± 35 ± 53	26 ± 0 ± 6 ± 1	2.7 ± 0.1 ± 1.9 ± 0.3	–
$Z/\gamma^*(\to e^+e^-)$+jets	–	–	–	–
Multijet	6400 ± 90 ± 5500	200 ± 20 ± 200	–	–
$t\bar{t}$ + single t	2660 ± 60 ± 530	120 ± 10 ± 20	7 ± 3 ± 1	1.2 ± 1.2 ± 0.2
Dibosons	815 ± 9 ± 163	83 ± 3 ± 17	14 ± 1 ± 3	3 ± 1 ± 1
Non-collision background	640 ± 40 ± 60	22 ± 7 ± 2	–	–
Total background	344400 ± 900 ± 2200 ± 12600	25600 ± 240 ± 500 ± 900	2180 ± 70 ± 120 ± 100	380 ± 30 ± 60 ± 30
Data	350932	25515	2353	268

Table 2: Number of observed events and predicted background events, including statistical and systematic uncertainties. The statistical uncertainties for data and MC simulation are shown separately. In the total background prediction the first quoted uncertainty reflects the contribution from the statistical uncertainty in the data in the control regions affecting the electroweak background estimation, the second represents the MC statistical uncertainty, and the third includes the rest of systematic uncertainties. In SR3 and SR4 selections the MC statistical uncertainty dominates. The background uncertainties in SR1 and SR2 selections are dominated by the rest of systematic uncertainties.

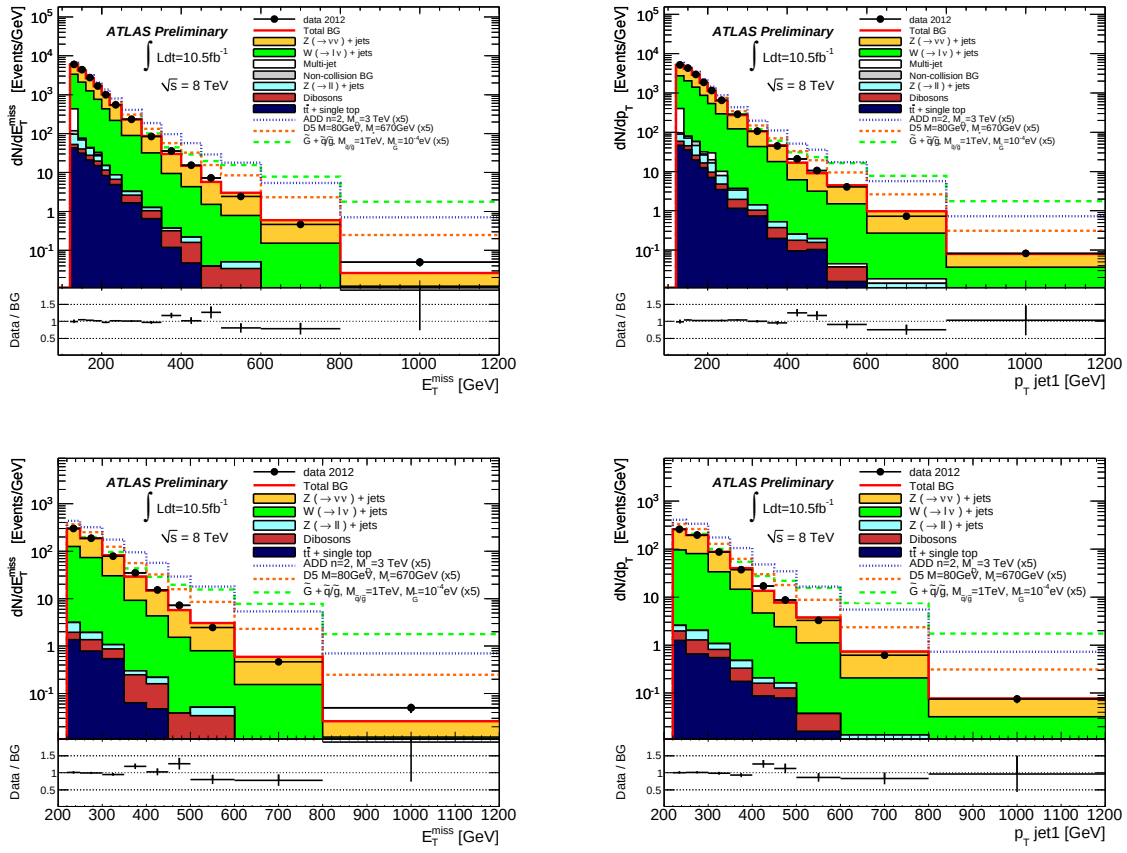

Figure 6: Measured leading jet p_{T} and $E_{\mathrm{T}}^{\mathrm{miss}}$ distributions (black dots) in the SR1 (top) and SR2 (bottom) signal regions compared to the predictions for SM backgrounds (histograms). Only statistical uncertainties are shown. For illustration purposes, the impact of different ADD, WIMP, and GMSB scenarios are included.

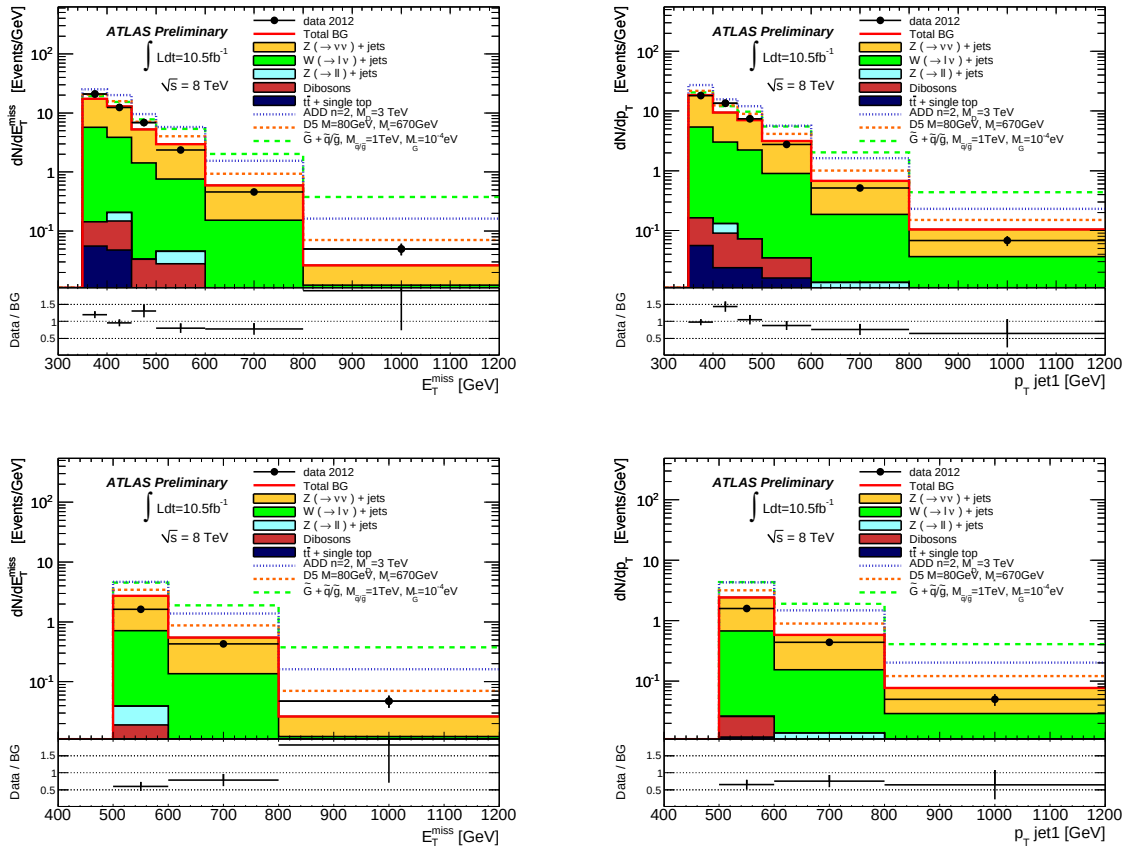

Figure 7: Measured leading jet p_{T} and $E_{\mathrm{T}}^{\mathrm{miss}}$ distributions (black dots) in the SR3 (top) and SR4 (bottom) signal regions compared to the predictions for SM backgrounds (histograms). Only statistical uncertainties are shown. For illustration purposes, the impact of different ADD, WIMP, and GMSB scenarios are included.

SR1 and betweeen 6% and 14% in SR4. Systematic uncertainties due to PDFs are evaluated using the Hessian method [54]. They result in uncertainties on the signal yields that vary between 6% to 11% for SR1 and as n increases, and between 8% and 12% for SR4. Finally, variations of the renormalization and factorization scales by factors of two and one-half introduce a 25% to 47% uncertainty on the signal yields with increasing n and jet p_{T} and $E_{\mathrm{T}}^{\mathrm{miss}}$ requirements. All together, this results in total uncertainties between 27% and 50% on the predicted signal yields.

95% CL limits on ADD model using LO signal cross sections						
n extra-	95% CL observed limit on M_D [TeV]			95% CL expected limit on M_D [TeV]		
dimensions	$+1\sigma$(theory)	Nominal	-1σ(theory)	$+1\sigma$	Nominal	-1σ
2	+0.32	3.88	−0.42	−0.36	4.24	+0.39
3	+0.21	3.16	−0.29	−0.24	3.39	+0.46
4	+0.16	2.84	−0.27	−0.16	3.00	+0.20
5	+0.16	2.65	−0.27	−0.13	2.78	+0.15
6	+0.13	2.58	−0.23	−0.11	2.69	+0.11

Table 3: The 95% CL observed and expected limits on M_D as a function of the number of extra-dimensions n for the SR3 selection and considering LO signal cross sections. The impact of the $\pm1\sigma$ theoretical uncertainty on the observed limits and the expected $\pm1\sigma$ range of limits in the absence of a signal are also given.

Figure 8 shows, for the SR3 selection, the ADD $\sigma \times A \times \epsilon$ as a function of M_D for $n = 2$ and $n = 6$ and corresponding to LO theoretical predictions. For comparison, the model-independent 95% CL limits are shown. Expected and observed 95% CL lower limits are set on the value of M_D as a function of the number of extra dimensions considered in the ADD model. The CL_s approach is used, including statistical and systematic uncertainties. For the latter, the uncertainties on the signal acceptance times efficiency, the background predictions, and the luminosity are considered, and correlations between systematic uncertainties on signal and background predictions are taken into account. In addition, observed limits are computed taking into account the $\pm1\sigma$ LO theoretical uncertainty. The signal region SR3 provides the best expected limits and is used to obtained the final results. Values of M_D below 3.88 TeV ($n = 2$), 3.16 TeV ($n = 3$), 2.84 TeV ($n = 4$), 2.65 TeV ($n = 5$), and 2.58 TeV ($n = 6$) are excluded at 95% CL. The observed limits decrease by 10% after considering the -1σ uncertainty from PDFs, scale variations, and parton shower modeling in the ADD theoretical predictions (see Table 3). These results do not supersede the 95% CL limits obtained in the previous analysis based on 7 TeV data [12]. The limits on M_D are not improved (except in the case of $n = 6$) due to the increase of the SM background levels and the lack of sufficient statistics in the MC samples employed for the background predictions. As discussed in [12], the analysis probes the phase space region with $\hat{s} > M_D^2$, where $\sqrt{\hat{s}}$ is the center-of-mass energy of the hard interaction. This region is sensitive to the unknown ultraviolet behavior of the effective theory.

6.2 WIMP production

Systematic uncertainties on WIMP pair production are treated similarly to those of the ADD limits, except for the PDF and ISR/FSR uncertainties. The former are determined using CTEQ6M error sets for the relative uncertainty around the CTEQ6L1 central value. The ISR/FSR uncertainties are estimated differently in a way that is appropriate for the high-p_{T} ISR/FSR regime probed here: a WIMP pair recoils against a high-p_{T} ISR/FSR jet, whereas for ADD, additional low-p_{T} ISR/FSR jets dominate the uncertainty due to the impact of the jet veto.

The experimental uncertainties due to jet and $E_{\mathrm{T}}^{\mathrm{miss}}$ energy scale and resolution lead to 1–10% uncer-

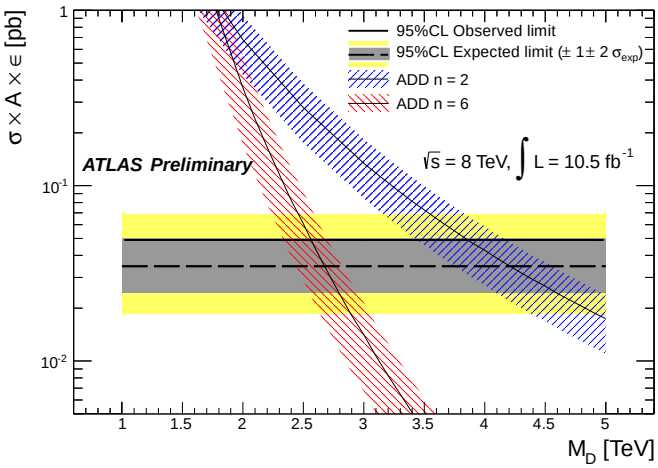

Figure 8: The predicted ADD $\sigma \times A \times \epsilon$ for the SR3 selection as a function of M_D for $n = 2$ and $n = 6$, where bands represent the uncertainty on the theory. For comparison, the model-independent observed (solid line) and expected (dashed line) 95% CL limits on $\sigma \times A \times \epsilon$ are shown. The shaded areas around the expected limit indicate the expected $\pm 1\sigma$ and $\pm 2\sigma$ ranges of limits in the absence of a signal.

tainties on the WIMP event yield depending on the WIMP mass and the effective operator considered. Other experimental uncertainties affecting the event yield are associated with the trigger efficiency (1%) and the luminosity measurement (3.6%). The ISR/FSR uncertainties are estimated by varying the jet matching scale between 5 and by a factor of one half and two. Moreover, the α_s scale is varied in within a range that is consistent with experimental data [55]. The resulting uncertainties on $\sigma \times A$, added in quadrature, are 3% for the matching scale and at most 8% for α_s. A negligible dependence of the ISR/FSR uncertainties on the choice of effective operator is found. PDF uncertainties mostly impact the signal cross section and hardly impact the acceptance. They are found to depend on the effective operator chosen. For D5, uncertainties ranging from 7% for the 80 GeV mass point to 30% for 1000 GeV WIMP mass are found. The uncertainties for D11 range from 25% for 80 GeV to 88% for 1000 GeV. Finally, the systematic uncertainties from the factorisation and renormalisation scales are determined by varying these scales simultaneously between twice and half their default value. Uncertainties of 10% are found for D5 and 30% for D11. The axial operator D8 exhibits the same kinematic behavior as D5 and only differs in cross section, all systematic uncertainties of D5 are hence used for D8, too.

Figure 9 shows the 90% CL lower limits on the suppression scale M_*, for all operators probed as a function of WIMP mass m_χ. These limits on M_* are derived from the cross-section limits at a given mass m_χ. The values displayed are for the signal region with the best expected limits, SR3. The lower limits are based on simulation samples produced for m_χ of 80, 400, and 1000 GeV. Extrapolations are shown down to $m_\chi = 10$ GeV. These are valid since there is negligible change in cross section or kinematic distributions at the LHC for low-mass WIMPs. For D8, the M_* limits are calculated using the D5 acceptances (as they are identical) together with D8 production cross sections. As before, the central values of observed and expected limits on M_* are displayed taking into account experimental but not theoretical uncertainties. The effect of ± 1 and 2σ variations on the expected limit due to statistical fluctuations and experimental uncertainties are shown as grey and blue bands. The impact of the theoretical uncertainties is represented by dotted red $\pm 1\sigma$ lines on either side of the observed limit. The nominal observed limit line excluding theoretical uncertainties is the final result. All values of the observed lower limits on the

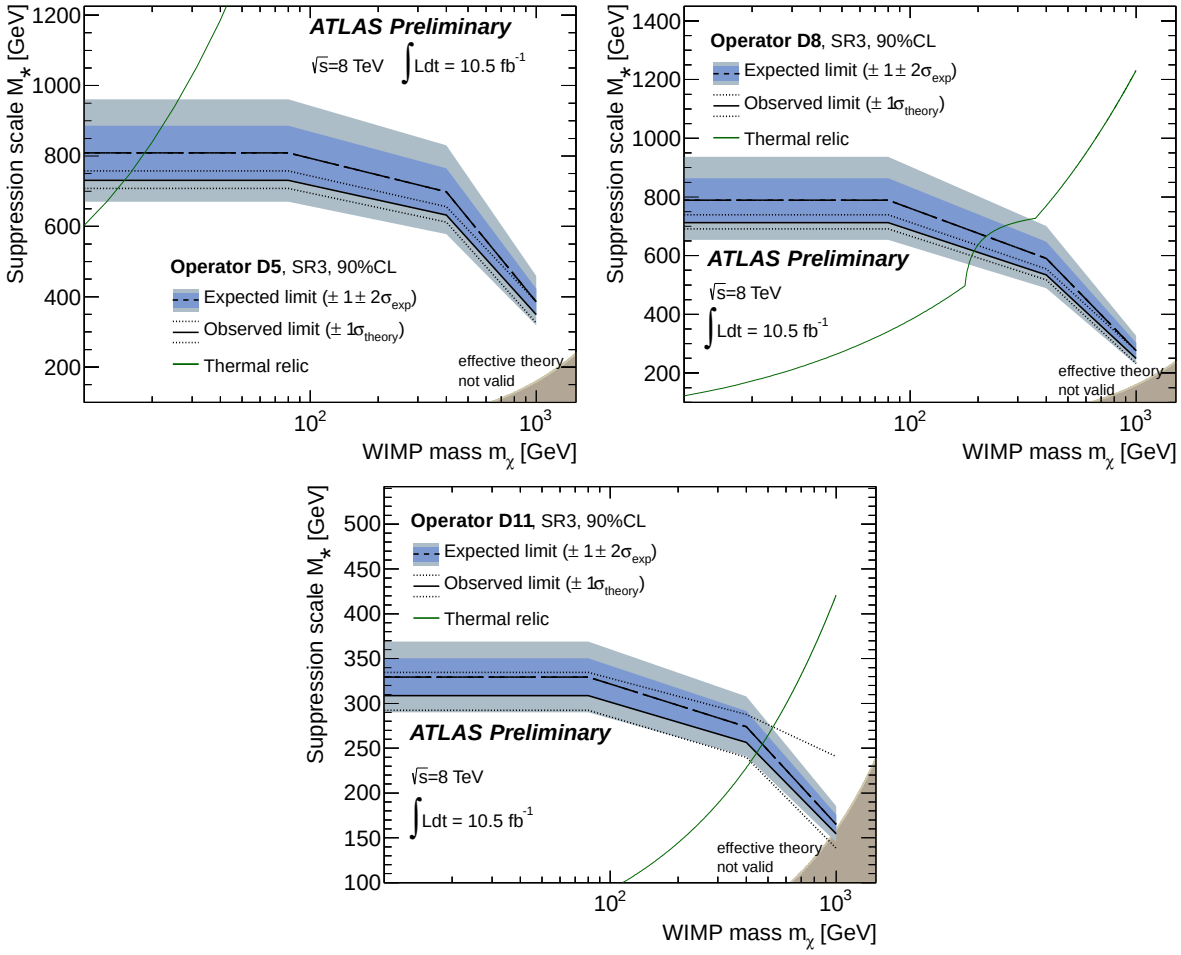

Figure 9: The 90% CL lower limits on M_* for different masses of χ. Observed and expected limits including all but the theoretical signal uncertainties are shown as dashed black and red solid lines, respectively. The grey and blue bands around the expected limit are the ± 1 and 2σ variation expected from statistical fluctuations and experimental systematic uncertainties on SM and signal processes. The impact of the theoretical uncertainties is shown by the thin red dotted $\pm 1\sigma$ limit lines around the observed limit. The M_* values at which WIMPs of a given mass would result in the required relic abundance are shown as rising green lines (taken from [22]), assuming annihilation in the early universe proceeded exclusively via the given operator. The shaded light-grey regions in the bottom right corners indicate where the effective field theory approach breaks down [22]. The plots are based on the best expected limits, which correspond to SR3.

suppression scale M_* at 90% and 95% CL are listed in table 4. Compared to the previous analysis [12], the expected lower limits of D5 and D8 are now about 10% larger (more restrictive), whereas the expected lower limits of D11 remain unchanged. For the latter operator, D11, the results shown here do not supersede the previous analysis presented in ref. [12].

m_χ	D5	D8	D11
≤ 80	731 (704)	713 (687)	309 (301)
400	632 (608)	535 (515)	257 (250)
1000	349 (336)	250 (240)	155 (151)

Table 4: The 90% (95%) CL observed lower limits on the suppression scale M_* as a function of WIMP mass m_χ. All values are given in GeV and correspond to the nominal observed limit excluding theoretical uncertainties. The signal region with the best expected limits, SR3, is quoted in all cases. Note that compared to the previous analysis at center of mass energies of $\sqrt{s} = 7$ TeV [12], the limits of D5 and D8 are now about 10% larger and hence more restrictive. For D11, the result does not improve the previous analysis.

The light-grey shaded regions in Figure 9 indicate where the effective field theory approach for WIMP pair production breaks down [22] (bottom-right corner in all plots). The M_* limits set in this analysis are above these bounds. No further measures are taken to ensure that the energy transfer in monojet events in this dataset remains in the valid region of the effective field theory. Such a region of validity cannot be defined without precise knowledge of the BSM physics, over which the effective operators integrate.

Figure 9 also includes *thermal relic* lines (taken from [22]) which correspond to a coupling, set by M_*, of WIMPs to quarks or gluons such that WIMPs have the correct relic abundance as measured by the WMAP satellite [56], in the absence of any other interaction than the one considered. Under the assumption that DM is entirely composed of thermal relics, ATLAS limits exceeding the observed thermal relic density exclude the case where DM annihilates exclusively to SM particles via the corresponding operator. Should thermal relic WIMPs exist with a mass at which the observed limit is above the thermal relic line, there would have to be other annihilation channels or annihilation via other operators in order to be consistent with the WMAP measurements.

6.3 Gravitino production

The results are expressed in terms of 95% CL limits on the cross section for the associated production of a gravitino and a gluino or a squark, for which the SR3 signal region is employed. As already discussed, a SUSY simplified model is used for which the gluino and squark decays lead to a gravitino and a gluon or a quark, respectively, producing a monojet signature in the final state. Squark and gluino masses up to 2.6 TeV are considered. The $A \times \epsilon$ for the SUSY signal depends on the mass of the squark or gluino in the final state and also on the relation between squark and gluino masses. As an example, in the case of squark and gluinos degenerate in mass ($m_{\tilde{g}} = m_{\tilde{q}}$), the signal $A \times \epsilon$ for the SR3 selection criteria is of the order of 30% for squark and gluino masses of about $1 - 2$ TeV.

The systematic uncertainties on the SUSY signal yields are determined as in the case of ADD and WIMP models. Experimental uncertainties related to the jet and $E_{\mathrm{T}}^{\mathrm{miss}}$ scales and resolutions introduce uncertainties in the signal yields that vary between 2% and 16% for different squark and gluino masses. A 1% uncertainty on the simulated trigger efficiency and a 3.6% uncertainty on the integrated luminosity are included. Uncertainties related to the modeling of ISR and FSR are determined using simulated samples

with modified parton shower parameters and translate into a 5% to 10% uncertainty on the signal yields in the SR3 region, depending on the squark and gluino masses. Systematic uncertainties due to PDFs result in uncertainties on the signal yields that vary between 5% and 60% for squark and gluino masses increasing from 50 GeV and 2.6 TeV. Finally, variations of the renormalization and factorization scales by factors of two and one-half introduce a 15% to 35% uncertainty on the signal yields with increasing squark and gluino masses.

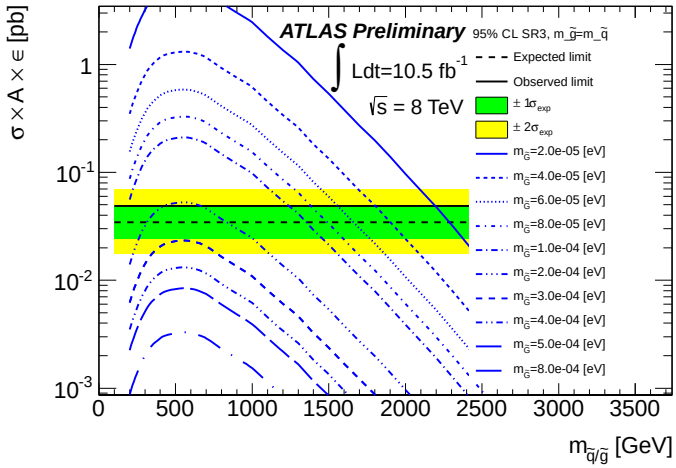

Figure 10: Cross section times acceptance times efficiency for the gravitino+squark/gluino production as a function of the squark/gluino mass in the case of degenerate squark and gluinos. Different values for the gravitino mass are considered and the predictions are compared with model-independent limits.

Figure 10 presents, for the case of degenerate squark and gluinos, the $\sigma \times A \times \epsilon$ as a function of the squark/gluino mass for different gravitino masses. For comparison, the model-independent 95% CL limits are shown. Expected and observed 95% CL limits on the gravitino-squark/gluino mass plane are presented in Figure 11, and are computed using the same procedure as in the case of the ADD and WIMPs models. Gravitino masses below $1{\cdot}10^{-4}$ eV ($4{\cdot}10^{-5}$ eV) are excluded at 95% CL for squark/gluino masses of 500 GeV (1.7 TeV). These results significantly improve previous results at LEP and the Tevatron and constitute the best bounds on the gravitino mass to date. For very high squark/gluino masses the NWA employed is violated since the partial width for the gluino and squark to decay into a gravitino and a parton becomes more than 25% of its mass and other decay channels should be considered. Finally, limits on the gravitino mass are also computed in the case of non-degenerate squarks and gluinos. Scenarios with $m_{\tilde{g}} = 4 \cdot m_{\tilde{q}}$, $m_{\tilde{g}} = 2 \cdot m_{\tilde{q}}$, $m_{\tilde{g}} = 1/2 \cdot m_{\tilde{q}}$, and $m_{\tilde{g}} = 1/4 \cdot m_{\tilde{q}}$ are explored in Figure 12, where 95% CL limits on the gravitino mass are presented as a function of the squark mass. In this case, 95% CL lower bounds on the gravitino mass in the range between $3 \cdot 10^{-4}$ eV and $3 \cdot 10^{-5}$ eV are set depending on the squark and gluino masses.

7 Summary and conclusions

In summary, we report results on the search for new phenomena in events with an energetic jet and large missing transverse momentum in proton-proton collisions at $\sqrt{s} = 8$ TeV at the LHC, based on ATLAS data corresponding to an integrated luminosity of 10.5 fb^{-1}. The measurements are in agreement with the SM predictions for the background. The results are translated into model-independent 95% confidence level upper limits on $\sigma \times A \times \epsilon$. The results are also presented in terms of new limits on the production of

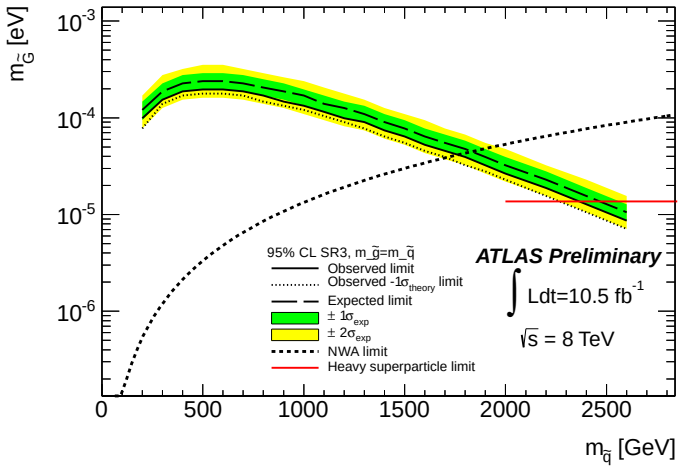

Figure 11: Observed (solid line) and expected (dashed line) 95% CL lower limits on the gravitino mass as a function of the squark mass for degenerate squark/gluino masses. The dotted line indicates the impact on the observed limit of the $\pm 1\sigma$ LO theoretical uncertainty. The shaded bands around the expected limit indicate the expected $\pm 1\sigma$ and $\pm 2\sigma$ ranges of limits in the absence of a signal. The dashed-dotted line defines the validity of the narrow-width approximation (see body of the text). The solid red line denotes the current limit from LEP [27] on the gravitino mass assuming very heavy squarks/gluino.

light grativinos in association with gluinos or scalar quarks in a gauge-mediated supersymmetric model, leading to the best lower bound to date on the gravitino mass. In addition, 95% CL limits on M_D versus the number of extra spatial dimensions, in the ADD LED model, and on the suppression scale M_* versus the WIMP mass, for the pair production of dark matter candidates, are presented that only partially supersede previous results.

References

[1] OPAL Collaboration, G. Abbiendi et al., *Photonic events with missing energy in e^+e^- collisions at $\sqrt{s}$ = 189 GeV*, Eur.Phys.J. **C18** (2000) 253–272, arXiv:hep-ex/0005002 [hep-ex].

[2] ALEPH Collaboration, A. Heister et al., *Single photon and multiphoton production in e^+e^- collisions at $\sqrt{s}$ up to 209 GeV*, Eur.Phys.J. **C28** (2003) 1–13.

[3] L3 Collaboration, P. Achard et al., *Single photon and multiphoton events with missing energy in e^+e^- collisions at LEP*, Phys.Lett. **B587** (2004) 16–32, arXiv:hep-ex/0402002 [hep-ex].

[4] DELPHI Collaboration, J. Abdallah et al., *Photon events with missing energy in e^+e^- collisions at $\sqrt{s}$ = 130 GeV to 209 GeV*, Eur.Phys.J. **C38** (2005) 395–411, arXiv:hep-ex/0406019 [hep-ex].

[5] D0 Collaboration, V. Abazov et al., *Search for large extra dimensions via single photon plus missing energy final states at $\sqrt{s}$ = 1.96 TeV*, Phys.Rev.Lett. **101** (2008) 011601, arXiv:0803.2137 [hep-ex].

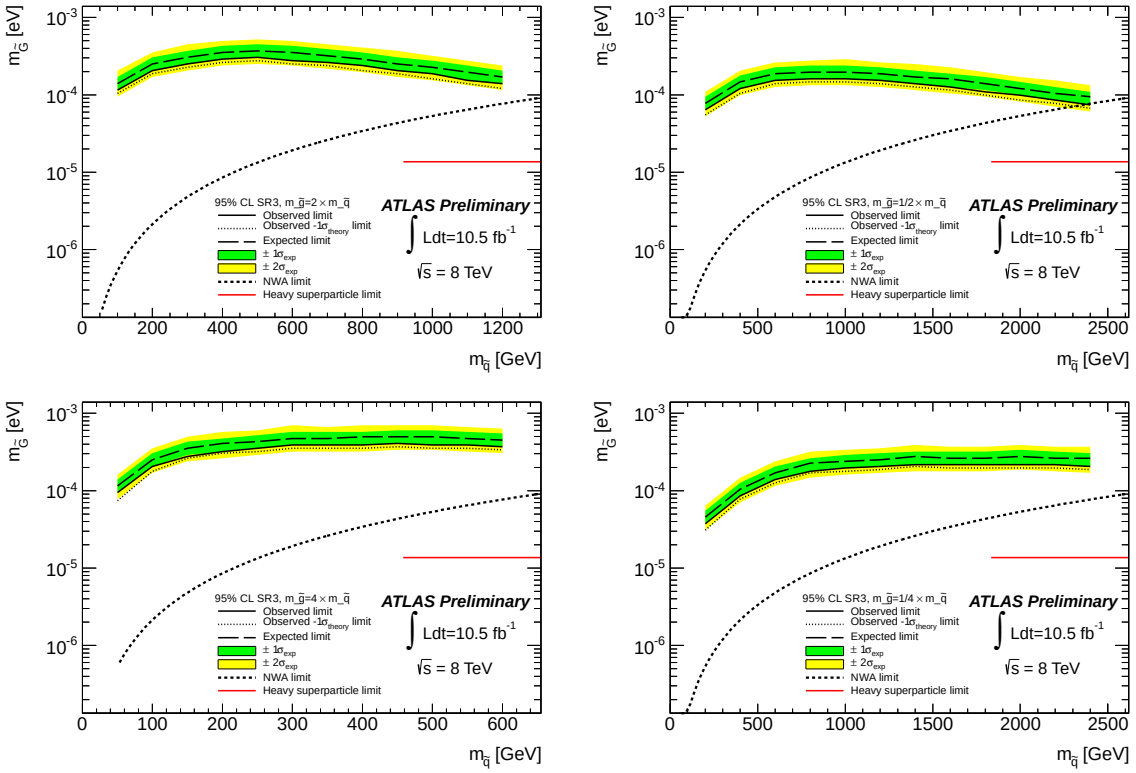

Figure 12: Observed (solid line) and expected (dashed line) 95% CL lower limits on the gravitino mass as a function of the squark mass for non-degenerate squark/gluino masses and different squark/gluino mass configurations. The dotted line indicates the impact on the observed limit of the $\pm 1\sigma$ LO theoretical uncertainty. The shaded bands around the expected limit indicate the expected $\pm 1\sigma$ and $\pm 2\sigma$ ranges of limits in the absence of a signal. The dashed-dotted line defines the validity of the narrow-width approximation (see body of the text). The solid red line denotes the current limit from LEP [27] on the gravitino mass assuming very heavy squarks/gluino.

[6] CDF Collaboration, T. Aaltonen et al., *Search for large extra dimensions in final states containing one photon or jet and large missing transverse energy produced in $p\bar{p}$ collisions at $\sqrt{s} = 1.96$ TeV*, Phys.Rev.Lett. **101** (2008) 181602, arXiv:0807.3132 [hep-ex].

[7] CDF Collaboration, T. Aaltonen et al., *A Search for dark matter in events with one jet and missing transverse energy in $p\bar{p}$ collisions at $\sqrt{s} = 1.96$ TeV*, Phys.Rev.Lett. **108** (2012) 211804, arXiv:1203.0742 [hep-ex].

[8] CMS Collaboration, *Search for New Physics with a Mono-Jet and Missing Transverse Energy in pp Collisions at $\sqrt{s} = 7$ TeV*, Phys.Rev.Lett. **107** (2011) 201804, arXiv:1106.4775 [hep-ex].

[9] CMS Collaboration, *Search for dark matter and large extra dimensions in monojet events in pp collisions at $\sqrt{s} = 7$ TeV*, JHEP **1209** (2012) 094, arXiv:1206.5663 [hep-ex].

[10] CMS Collaboration, *Search for Dark Matter and Large Extra Dimensions in pp Collisions Yielding a Photon and Missing Transverse Energy*, Phys.Rev.Lett. **108** (2012) 261803, arXiv:1204.0821 [hep-ex].

[11] ATLAS Collaboration, *Search for new phenomena with the monojet and missing transverse momentum signature using the ATLAS detector in $\sqrt{s}$ = 7 TeV proton-proton collisions*, Phys.Lett. **B705** (2011) 294–312, arXiv:1106.5327 [hep-ex].

[12] ATLAS Collaboration, *Search for dark matter candidates and large extra dimensions in events with a jet and missing transverse momentum with the ATLAS detector*, submitted to JHEP , arXiv:1210.4491 [hep-ex].

[13] ATLAS Collaboration, *Search for dark matter candidates and large extra dimensions in events with a photon and missing transverse momentum in pp collision data at $\sqrt{s}$ = 7 TeV with the ATLAS detector*, submitted to Phys. Rev. Lett. , arXiv:1209.4625 [hep-ex].

[14] CDF Collaboration, T. Affolder et al., *Limits on gravitino production and new processes with large missing transverse energy in $p\bar{p}$ collisions at $\sqrt{s}$ = 1.8 TeV*, Phys.Rev.Lett. **85** (2000) 1378–1383, arXiv:hep-ex/0003026 [hep-ex].

[15] N. Arkani-Hamed, S. Dimopoulos, and G. Dvali, *The Hierarchy problem and new dimensions at a millimeter*, Phys.Lett. **B429** (1998) 263–272, arXiv:hep-ph/9803315 [hep-ph].

[16] G. Bertone, D. Hooper, and J. Silk, *Particle dark matter: Evidence, candidates and constraints*, Phys.Rept. **405** (2005) 279–390, arXiv:hep-ph/0404175 [hep-ph].

[17] XENON100 Collaboration, E. Aprile et al., *Dark Matter Results from 225 Live Days of XENON100 Data*, arXiv:1207.5988 [astro-ph.CO].

[18] CDMS Collaboration, Z. Ahmed et al., *Results from a Low-Energy Analysis of the CDMS II Germanium Data*, Physical Review Letters **106** (2011).

[19] CoGeNT Collaboration, C. Aalseth et al., *Results from a Search for Light-Mass Dark Matter with a P-type Point Contact Germanium Detector*, Phys.Rev.Lett. **106** (2011) 131301, arXiv:1002.4703 [astro-ph.CO].

[20] PICASSO Collaboration, S. Archambault et al., *Constraints on Low-Mass WIMP Interactions on ^{19}F from PICASSO*, Phys.Lett. **B711** (2012) 153–161, arXiv:1202.1240 [hep-ex].

[21] M. Felizardo, T. Girard, T. Morlat, A. Fernandes, A. Ramos, et al., *Final Analysis and Results of the Phase II SIMPLE Dark Matter Search*, Phys.Rev.Lett. **108** (2012) 201302, arXiv:1106.3014 [astro-ph.CO].

[22] J. Goodman, M. Ibe, A. Rajaraman, W. Shepherd, T. M. Tait, et al., *Constraints on Dark Matter from Colliders*, Phys.Rev. **D82** (2010) 116010, arXiv:1008.1783 [hep-ph].

[23] G. Giudice and R. Rattazzi, *Theories with gauge mediated supersymmetry breaking*, Phys.Rept. **322** (1999) 419–499, arXiv:hep-ph/9801271 [hep-ph].

[24] P. Fayet, *Mixing Between Gravitational and Weak Interactions Through the Massive Gravitino*, Phys.Lett. **B70** (1977) 461.

[25] R. Casalbuoni, S. De Curtis, D. Dominici, F. Feruglio, and R. Gatto, *A GRAVITINO - GOLDSTINO HIGH-ENERGY EQUIVALENCE THEOREM*, Phys.Lett. **B215** (1988) 313.

[26] M. Klasen and G. Pignol, *New Results for Light Gravitinos at Hadron Colliders: Tevatron Limits and LHC Perspectives*, Phys.Rev. **D75** (2007) 115003, arXiv:hep-ph/0610160 [hep-ph].

[27] LEP2 SUSY Working Group Collaboration, *Single Photons, 183-208 GeV*, http://lepsusy.web.cern.ch/lepsusy/www/photons/single/single_public_summer04.html .

[28] ATLAS Collaboration, *The ATLAS Experiment at the CERN Large Hadron Collider*, JINST **3** (2008) S08003.

[29] ATLAS Collaboration, *Expected Performance of the ATLAS Experiment - Detector, Trigger and Physics*, arXiv:0901.0512 [hep-ex].

[30] M. Cacciari, G. P. Salam, and G. Soyez, *The anti-k_t jet clustering algorithm*, JHEP **04** (2008) 063, arXiv:0802.1189 [hep-ph].

[31] ATLAS Collaboration, *Jet energy measurement with the ATLAS detector in proton-proton collisions at $\sqrt{s}$ = 7 TeV*, accepted for publication in Eur.Phys.J.C , arXiv:1112.6426 [hep-ex].

[32] ATLAS Collaboration, *Performance of Missing Transverse Momentum Reconstruction in Proton-Proton Collisions at 7 TeV with ATLAS*, Eur.Phys.J. **C72** (2012) 1844, arXiv:1108.5602 [hep-ex].

[33] ATLAS Collaboration, *Measurement of the inclusive $W^{\pm}$ and $Z/\gamma^{\star}$ cross sections in the electron and muon decay channels in pp collisions at $\sqrt{s}$ = 7 TeV with the ATLAS detector*, Phys. Rev. D85, **072004** (2012), arXiv:1109.5141 [hep-ex].

[34] ATLAS Collaboration, *Performance of the ATLAS Trigger System in 2010*, Eur.Phys.J. **C72** (2012) 1849, arXiv:1110.1530 [hep-ex].

[35] ATLAS Collaboration, *Selection of jets produced in proton-proton collisions with the ATLAS detector using 2011 data*, ATLAS-CONF-2012-020 (2012).

[36] M. Mangano *et al.*, *ALPGEN, a generator for hard multiparton processes in hadronic collisions*, JHEP **07** (2003) 001, arXiv:hep-ph/0206293.

[37] G. Corcella *et al.*, *HERWIG 6: An event generator for hadron emission reactions with interfering gluons (including supersymmetric processes)*, JHEP **01** (2001) 010, arXiv:hep-ph/0011363.

[38] J. Butterworth, J. R. Forshaw, and M. Seymour, *Multiparton interactions in photoproduction at HERA*, Z.Phys. **C72** (1996) 637–646, arXiv:hep-ph/9601371 [hep-ph].

[39] J. Pumplin, D. Stump, J. Huston, H. Lai, P. M. Nadolsky, et al., *New generation of parton distributions with uncertainties from global QCD analysis*, JHEP **0207** (2002) 012, arXiv:hep-ph/0201195 [hep-ph].

[40] K. Melnikov and F. Petriello, *Electroweak gauge boson production at hadron colliders through $O(\alpha_s^2)$*, Phys.Rev. **D74** (2006) 114017, arXiv:hep-ph/0609070 [hep-ph].

[41] R. Gavin, Y. Li, F. Petriello, and S. Quackenbush, *FEWZ 2.0: A code for hadronic Z production at next-to-next-to-leading order*, Comput.Phys.Commun. **182** (2011) 2388–2403, arXiv:1011.3540 [hep-ph].

[42] S. Frixione and B. R. Webber, *The MC@NLO 3.2 event generator*, arXiv:hep-ph/0601192 [hep-ph].

[43] H.-L. Lai, M. Guzzi, J. Huston, Z. Li, P. M. Nadolsky, et al., *New parton distributions for collider physics*, Phys.Rev. **D82** (2010) 074024, arXiv:1007.2241 [hep-ph].

[44] T. Gleisberg, S. Hoeche, F. Krauss, M. Schonherr, S. Schumann, et al., *Event generation with SHERPA 1.1*, JHEP **0902** (2009) 007, arXiv:0811.4622 [hep-ph].

[45] A. Sherstnev and R. Thorne, *Parton Distributions for LO Generators*, Eur.Phys.J. **C55** (2008) 553–575, arXiv:0711.2473 [hep-ph].

[46] A. Martin, W. Stirling, R. Thorne, and G. Watt, *Parton distributions for the LHC*, Eur.Phys.J. **C63** (2009) 189–285, arXiv:0901.0002 [hep-ph].

[47] T. Sjostrand, S. Mrenna, and P. Z. Skands, *PYTHIA 6.4 Physics and Manual*, JHEP **0605** (2006) 026, arXiv:hep-ph/0603175 [hep-ph].

[48] P. M. Nadolsky, H.-L. Lai, Q.-H. Cao, J. Huston, J. Pumplin, et al., *Implications of CTEQ global analysis for collider observables*, Phys.Rev. **D78** (2008) 013004, arXiv:0802.0007 [hep-ph].

[49] J. Alwall, M. Herquet, F. Maltoni, O. Mattelaer, and T. Stelzer, *MadGraph 5 : Going Beyond*, JHEP **1106** (2011) 128, arXiv:1106.0522 [hep-ph].

[50] K. Mawatari and Y. Takaesu, *HELAS and MadGraph with goldstinos*, Eur.Phys.J. **C71** (2011) 1640, arXiv:1101.1289 [hep-ph].

[51] ATLAS Collaboration, *The ATLAS Simulation Infrastructure*, Eur. Phys. J. **C70** (2010) 823–874, arXiv:1005.4568 [physics.ins-det].

[52] GEANT4 Collaboration, S. Agostinelli *et al.*, *GEANT4: A simulation toolkit*, Nucl. Instrum. Meth. **A506** (2003) 250–303.

[53] A. L. Read, *Presentation of search results: The CL_s technique*, J.Phys.G **G28** (2002) 2693–2704.

[54] J. Pumplin, D. Stump, R. Brock, D. Casey, J. Huston, et al., *Uncertainties of predictions from parton distribution functions. 2. The Hessian method*, Phys.Rev. **D65** (2001) 014013, arXiv:hep-ph/0101032 [hep-ph].

[55] P. Z. Skands, *Tuning Monte Carlo Generators: The Perugia Tunes*, Phys.Rev. **D82** (2010) 074018, arXiv:1005.3457 [hep-ph].

[56] WMAP Collaboration, E. Komatsu et al., *Seven-Year Wilkinson Microwave Anisotropy Probe (WMAP) Observations: Cosmological Interpretation*, Astrophys.J.Suppl. **192** (2011) 18, arXiv:1001.4538 [astro-ph.CO].